Estimation of Mud and Sand Fractions and Total Concentration From Coupled Optical-Acoustic Sensors

Duc Tran[1,2] , **Matthias Jacquet[1]**, **Stuart Pearson[3]** , **Bram Van Prooijen[3]**, and **Romaric Verney[1]**

[1]IFREMER, DYNECO/DHYSED, Plouzané, France, [2]Current: Royal Belgian Institute of Natural Sciences, Brussels, Belgium, [3]Faculty of Civil Engineering and Geosciences, Delft University of Technology, Delft, The Netherlands

Abstract Optical turbidity and acoustic sensors have been widely used in laboratory experiments and field studies to investigate suspended particulate matter concentration over the last four decades. Both methods face a serious challenge as laboratory and in-situ calibrations are usually required. Furthermore, in coastal and estuarine environments, the coexistence of mud and sand often results in multimodal particle size distributions, amplifying erroneous measurements. This paper proposes a new approach of combining a pair of optical turbidity-acoustic sensors to estimate the total concentration and sediment composition of a mud/sand mixture in an efficient way without an extensive calibration. More specifically, we first carried out a set of 54 bimodal size regime experiments to derive empirical functions of optical-acoustic signals, concentrations, and mud/sand fractions. The functionalities of these relationships were then tested and validated using more complex multimodal size regime experiments over 30 optical-acoustic pairs of 5 wavelengths (420, 532, 620, 700, 852 nm) and six frequencies (0.5, 1, 2, 4, 6, 8 MHz). In the range of our data, without prior knowledge of particle size distribution, combinations between optical wavelengths 620–700 nm and acoustic frequencies 4–6 MHz predict mud/sand fraction and total concentration with the variation <10% for the former and <15% for the later. The results also suggest that acoustic-acoustic signals could be combined to produce meaningful information regarding concentration and mud/sand fraction, while no useful knowledge could be extracted from a combination of optical-optical pairs. This approach therefore enables the robust estimation of suspended sediment concentration and composition, which is particularly practical in cases where calibration data is insufficient.

Plain Language Summary Crucial decisions to govern the development of an estuary, delta, or coastal zone often rely heavily on the knowledge of where sediment accumulates. Such knowledge primarily comes from long-term, high-frequency monitoring of the transport of mud and sand particles in the water column. Optical or acoustic sensors are usually used for this task. Optical/acoustic sensors emit a light/sound beam to the particles and then measure the strength of the reflecting signals to estimate the concentration of the suspension. Since particles with different shape, size, and density respond differently to the light/sound signals, intensive calibrations are required whenever there is a significant change in the water column, for example, during a tidal cycle, seasonal variations between summer and winter. To avoid these tedious calibrations processes, we experimentally show that combination of optical and acoustic sensors in one measurement will help to derive empirical functions which in turn allow us to estimate the ratio of mud/sand and total concentration.

1. Introduction

Accurate observation of suspended particulate matter concentration (SPMC) typically requires combinations of one or more optical turbidity and acoustic sensors with gravimetric measurements of filtered water samples (Bux et al., 2019; Fettweis et al., 2019; Sutherland et al., 2000). This is because both optical turbidity and acoustic sensors indirectly measure the backscattered signals of an optical beam or the acoustic backscatter as a proxy of SPMC. Conversely, the gravimetric measurements of filtered water samples directly provide the ground truth reference of SPMC. A regression model is then developed based on these indirect measurements and direct measurements of SPMC (Fettweis et al., 2019). Both direct or indirect measurements of SPMC have their own drawbacks. Physical water sampling is often impractical and expensive, particularly at high-frequencies over long periods for timeseries or vertical profile data collections. Optical turbidity and acoustic methods, on the other hand, provide high-resolution measurements. However, these two methods demand laboratory and *in-situ* calibration owing to the strong dependence of the backscattering characteristics on mineralogical compositions,

Validation: Duc Tran, Matthias Jacquet, Bram Van Prooijen, Romaric Verney
Visualization: Duc Tran, Stuart Pearson, Romaric Verney
Writing – original draft: Duc Tran
Writing – review & editing: Duc Tran, Matthias Jacquet, Stuart Pearson, Bram Van Prooijen, Romaric Verney

particle size, density and shape (Doxaran et al., 2016; Druine et al., 2018; Salehi & Strom, 2011; Slade et al., 2011). The backscattering signal is also influenced by the presence of salinity, bubbles and biological fouling (Bux et al., 2019; Downing, 2006; Haalboom et al., 2021; Sahin et al., 2017; Salehi & Strom, 2011). In practice, optical turbidity and acoustic measurements often combine with several *in-situ* or laboratory calibrations of water samples obtained from the field. For reliable and high fidelity data, it is suggested that sensors need to be re-calibrated with water samples when there are significant changes in SPM compositions and/or hydrodynamics conditions (Fettweis et al., 2019; Haalboom et al., 2021; Moura et al., 2011; Pearson et al., 2021). Hence, these methods require not only site-specific but also instrument-specific calibrations, adding another layer of difficulty and uncertainty to the inversion process.

Particles in suspension respond to both optical and acoustic signals via a similar mechanism, albeit to different degrees. Optical turbidity sensors illuminate a water sample volume with a light source, then the photodetectors convert the back (side)scatter intensity of the light in voltage or turbidity units (Downing, 2006; Fettweis et al., 2019). Similarly, acoustic sensors indirectly estimate concentration by quantifying the changes in back-scattered acoustic signals, in dB (Bux et al., 2019; Haalboom et al., 2021; Sahin et al., 2017). The peak sensitivity of acoustic backscatter signal to particle size occurs at upper limit of the Rayleigh regime at $2\pi r \lambda^{-1} \approx 1$ (Downing, 2006; Haalboom et al., 2021; Thorne & Hurther, 2014), where r is the particle radius and λ is the acoustic wavelength. For example, an Acoustic Doppler Velocimeter (ADV) working at 2 or 6 MHz will have the best performance with sand particles at sizes of 240 or 80 µm, respectively. For optical turbidity backscatter sensors, the light scattering and refractive index are largely dictated by the number of illuminated particles, or total illuminated areas (Downing, 2006), hence, the optical turbidity sensors are more sensitive to finer particles, that is, mud ($d_{50} < 63$ µm). If we combine both optical turbidity and acoustic sensors in one measurement of the same suspension we would thus "see" the mud better and "hear" the sand better. This allows us to gain deeper understanding about the suspension than we could if we only use a single type of sensor (Livsey et al., 2023; Pearson et al., 2021).

This study focuses on proposing a new method to use coupled optical-acoustic measurements to infer SPM compositions and concentrations without or with limited water sampling calibrations. As discussed above, optical backscattering signals are highly sensitive to mud, and acoustic backscattering signals are highly sensitive to sand particles, and vice versa. We further hypothesize that SPMC and composition can be differentiated and calculated based on such sensitivities and differences in behaviors of mud and sand to different types of signals, that is, optical and acoustic. The first objective of this paper is to investigate the possibility of combining a pair of optical turbidity and acoustic sensors to provide information about the mud/sand fraction and SPMC. To do so, we will quantify the sensitivity of a wide range of commercially available optical turbidity and acoustic sensors to the evolution of suspensions from mud-dominant to sand-dominant settings. More specifically, five optical turbidity and acoustic sensors will be used to cover the wavelengths from 420 to 852 nm and frequencies from 0.5 to 8 MHz, resulting in 30 different pairs of one wavelength and one frequency for each experiment. The second objective is to quantify at which wavelength/frequency the pair of optical turbidity and acoustic sensors will provide the most accurate estimation of SPMC at given concentration and particle size characteristics. Note that here and throughout the remainder of this paper, "wavelength" refers to optical wavelength, and "frequency" to acoustic frequency, unless noted otherwise.

2. Experimental Setup and Data Processing

2.1. Experimental Setup

Two sets of experiments were conducted to test and validate the hypothesis. The first set, the Quantification set Q_{set}, consisting of 54 experiments, was examined to derive empirical relationships between each pair of optical/ acoustic signal and mud/sand fraction (f_{mud}) and concentration. The second set, the Validation set (V_{set}) used six experiments to justify the applicability of such empirical relationships in predicting f_{mud} and SPMC of the suspension.

Table 1 shows the experimental conditions in Q_{set}. In this study, Bentonite and two particle sizes of sand were utilized to represent mud and sand. Preliminary experiments showed that flocculation occurred during the first two steps (task 1 and 2 in Table 1), resulting in an increase from clay primary particle size, $d_{50} = 5$ µm, to equilibrium floc size, $d_{50} \approx 40$ µm (Figure S1 in Supporting Information S1). The sands were sieved with sieve mesh 100–125

Table 1

Experimental Conditions and Procedure of the Quantification Set, Q_{set}

C [mg/L]	Bentonite/sand fraction (f_{mud}) [%]			Task	Time [min]
	100	75, 50, 25	0		
15	(pure mud)	(mixed Bentonite/sand)	(pure sand)	1. Bentonite stabilized in a beaker	0–30
25				2. Bentonite stabilized in DEXMES	30–60
50	Q1_100	Q1_75,50,25	Q1_0	3. Introduce sand in DEXMES	55
100	Or	Or	Or	4. Data recording	60–70
150	Q2_100	Q2_75,50,25	Q2_0	5. Water sampling	71–73
200				6. New sediment for the next step	Repeat task 1–5

Note. S1: sand particle size $d_{50} = 110$ μm. S2: sand particle size $d_{50} = 240$ μm. The notation one or two indicates S1 or S2 in the mixture.

μm and 200–250 μm to obtain sand S1 ($d_{50} = 110$ μm) and S2 ($d_{50} = 240$ μm), respectively. The particle size distributions of the mud and sands are provided in the supplemental information. Five ratios of mud/sand fractions, f_{mud}, were investigated: pure Bentonite ($f_{mud} = 100\%$), pure sand ($f_{mud} = 0\%$), and three intermediate mixtures: 75, 50, 25%. Hereafter, the suffixes 1 and 2 refer to the sand particle sizes of S1 ($d_{50} = 110$ μm) and S2 ($d_{50} = 240$ μm), respectively. The suffixes _100, _75, _50, _25, _0 refer to the fraction of Bentonite in suspension, or f_{mud}. For example, Q1_75 indicates the experiment from the quantification set, Q_{set}, in which the suspension consists of Bentonite and sand S1 with the ratio of mud/sand, f_{mud}, is 75%. For each SPM content condition, six concentrations were tested stepwise from 15 to 200 mg/L (Table 1). We processed the data from Q_{set} as three populations which are (a) **Q1**: pure Bentonite and all S1-related experiments (b) **Q2**: pure Bentonite and all S2-related experiments and (c) combination of Q1 and Q2 called **Q12**. In this study, there was only one pure Bentonite experiment; however, for consistency it was referred as Q1_100 in Q1 and Q2_100 in Q2, respectively.

Table 2 provides details of 6 additional experiments in V_{set}. It is noted that while Q_{set} is a bimodal particle size mixture, V_{set} is a multimodal particle size mixture. In fact, V_{set} was split in a way that either Bentonite, S1, or S2 was the dominant sediment in various mixture ratios among the three types of sediments at least once. Thus, results from V_{set} provide not only a higher range of concentrations but also an expanded range of f_{mud}. In Table 2, the numbers outside the parentheses refers to the targeted concentrations or Bentonite fraction, f_{mud}. The numbers inside the parentheses refer to the true values of the parameters. These numbers were often less than the targeted concentrations because the applied turbulent shear was not high enough to keep all the sand in suspension at the elevation of the sensors, especially S2 ($d_{50} = 240$ μm).

Table 3 summarizes all the optical and acoustic sensors used in this study. Specifically, the sensors are HydroScat-4 with four channels 852, 620, 532, 420 nm, Wetlabs_FLNTU 700 nm, Laser In-Situ Scattering and Transmissometery - Acoustic Backscatter Sensor (LISST-ABS) 8 MHz, Nortek Vector Acoustic Doppler Velocimeter (ADV) 6 MHz, AQUAscat-1000R with four transducers 4, 2, 1, and 0.5 MHz. In this study, the sensors were setup so that the measuring volume of each sensor was at a similar level, around 26–33 cm below the water surface (Figure 1).

The experiments were conducted in the DEXMES tank (Dispositif EXpérimental de quantification des Matières En Suspension), a novel device which was particularly designed for SPM experiments (Tran et al., 2021). DEXMES tank provides sufficient volume, approximately 1 m³, for several sensors to function concurrently. From a series of preliminary experiments, we found that the highest speed at which the impeller kept majority of sand in suspension and did not generate a noticeable amount of bubbles was 175 rotations per minute. Hence, in all experiments, the impeller was set at speed of 175 rotations per minute.

In general, the tank was filled with fresh water and left overnight to reach room temperature. An experiment was started with 30 min of high shearing to

Table 2

Experimental Conditions of the Validation Set, V_{set} x (y): Target (Measured). $d_{avg} = \sum_i^n d_i p_i$ Where d_i is the Particle Size of Size Fraction i, and p_i is the Percentage by Mass of Size Fraction i. i Denotes Be = 40, S1 = 110, or S2 = 240 μm

Run	C [mg/L]	Bentonite/sand fraction [%]			d_{avg} [μm]
		Be (40 μm)	S1 (110 μm)	S2 (240 μm)	
1	50 (46)	100 (100)	0 (0)	0 (0)	40
2	75 (68)	67 (67)	33 (33)	0 (0)	63
3	125 (103)	40 (44)	20 (21)	40 (35)	125
4	200 (174)	25 (26)	50 (54)	25 (20)	118
5	250 (191)	20 (23)	40 (45)	40 (32)	136
6	400 (330)	50 (54)	25 (31)	25 (15)	92

Table 3
A Summary of Working Conditions of all Sensors Used in This Study. Data From LISST-100X (Not Shown Here) is Used to Verify the Particle Size Distribution in Suspension, but is Not Paired With Other Sensors During the Data Analysis Process

	Sensor	Working Frequency [MHz]/Wavelength [nm]	Sampling Frequency [Hz]	Data output unit	Notation in text
Acoustic	LISST-ABS	8	1	mg/L	A_8
	ADV Vector	6	32	SNR - dB	A_6
	AQUAscat 1000R (Transducer 4 MHz)	4	32	Count	A_4
	AQUAscat 1000R (Transducer 2 MHz)	2	32	Count	A_2
	AQUAscat 1000R (Transducer 1 MHz)	1	32	Count	A_1
	AQUAscat 1000R (Transducer 0.5 MHz)	0.5	32	Count	$A_{0.5}$
Optical	HydroScat-4 (Channel 4)	852	1	m^{-1}	O_{852}
	Wetlabs_FLNTU	700	1	Count - > NTU	O_{700}
	HydroScat-4 (Channel 3)	620	1	m^{-1}	O_{620}
	HydroScat-4 (Channel 2)	532	1	m^{-1}	O_{532}
	HydroScat-4 (Channel 1)	420	1	m^{-1}	O_{420}

remove bubbles inside the tank. For mud, Bentonite was stabilized in suspension for 30 min in a 5 L beaker with a mixer before being introduced into DEXMES. Next, a 30 min mixing was applied to provide enough time for Bentonite particles to reach equilibrium floc size. Then, sand was added to the DEXMES tank, 5 min before data collection, to reach the targeted concentration. At the end of the 10 min recording step, one 1 L water sample was collected using a nozzle located at ≈25 cm below the water surface and 12 cm away from the wall of the tank. This procedure was repeated for all concentration levels (Table 1 and Figure 1). In V_{set}, for better quantification of the true fractions of Bentonite, S1, and S2 in suspension instead of one 1 L water sample, three 1 L water samples were collected and analyzed.

Note that the time for each task was carefully tested in a series of preliminary experiments to make sure (a) the flocculation time of the lowest concentration condition ($C = 15$ mg/L) was sufficient for particles to reach equilibrium floc size, verified with LISST-100X data, (b) the sand particles were evenly distributed throughout the DEXMES tank, verified with ADV and Wetlab data, and (c) there was sufficient preparation time for the next concentration step.

2.2. Data Processing

2.2.1. Optical and Acoustic Signal

All sensors started recording in real-time, continuous mode before any sediment was introduced into the tank until the last water sample was collected. For each examined condition, 10 min data was averaged and utilized in the analysis (Table 1). Preliminary experiments suggested that the numbers of spike/bad data points are negligible. Hence, there was no further transformation and/or correction of the output signals, except for Wetlabs_FLNTU where the output signal was converted from count to NTU as recommended by the Sea-Bird Scientific: NTU = 0.0484 (count - 50). Another note is that the LISST-ABS is used with its default (factory) concentration without calibration. Thus, even though the unit of the output from the LISST-ABS is mg/L, it is still "raw signal." In the present paper, we consider each transducer of the AQUAscat-1000R and each channel of the HydroScat-4 as individual sensor (Table 3). It is also noted that due to the nature of signal recording mechanisms, the relationships of ADV (SNR-dB) signal and SPMC or optical signal is a log-linear. Hence, in order to pair with ADV signal the concentration or optical data is converted via a $10\log_{10}()$
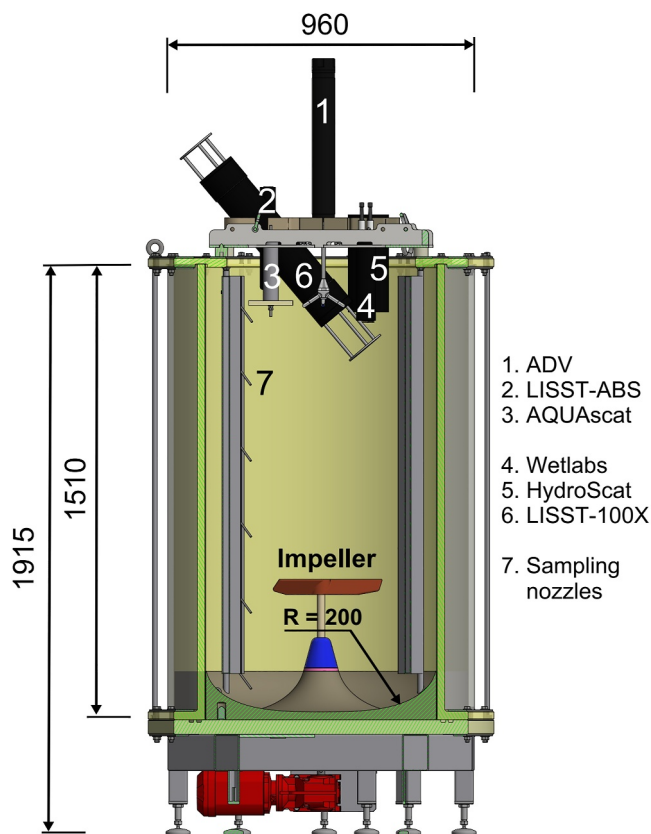

Figure 1. Experimental setup of the DEXMES tank (not to scale). Measuring volumes of all sensors were set at similar level as of water sampling nozzle, ≈25–26 cm below the water surface.

Figure labels:
960
1915
1510
1. ADV
2. LISST-ABS
3. AQUAscat
4. Wetlabs
5. HydroScat
6. LISST-100X
7. Sampling nozzles
Impeller
R = 200

function (Chmiel et al., 2018; Hoitink & Hoekstra, 2005; Salehi & Strom, 2011). Regarding AQUAscat-1000R sensor, AQUATEC suggested to use a quadratic regression between concentration and the backscatter signal (Equation 4—Aquatec Subsea Ltd (2012)). Subsequently, when pairing with optical or concentration data, AQUAscat signal is transformed to $(AQUAscat\_signal)^2$. The primary goal of this study is to investigate the behavior of optical/acoustic signals to different SPM concentrations and compositions. We have no intention to make a comparison between different commercial sensors, henceforth, the optical turbidity and acoustic sensors will be referred as their wavelengths or frequencies rather than by names or brands (last column in Table 3).

2.2.2. Water Sample

For each V_{set} condition, three 1 L water samples were collected. S2, S1, and Bentonite are separated by sieving through 125 and 63 μm sieves to obtain sand S2 and S1 on aluminum pans, and then filtered with a glass fiber filter to capture Bentonite, respectively. The separated sediments were dried in an oven at 50^oC in 24 hr and then weighed to measure mass concentration.

There are a few notes regarding water sample data. First, in Q_{set}, there were only two types of sediment, Bentonite and either S1 or S2, therefore we did not separate mud/sand in quantifying f_{mud} and total concentration in Q_{set}. Rather, the fraction and concentration of S1 or S2 in Q_{set} are acquired by subtracting the f_{mud} from the total concentration. This is because Bentonite never deposited within the DEXMES tank. Hence, what have left on the glass fiber filter must contain Bentonite and sand. Since we know exactly how much Bentonite we put into the tank and it always stayed in suspension, we assumed that mass of Bentonite should be constant in each run. Any changes in terms of concentration and/or fraction of mud/sand in Q_{set} were due to the deposition of sand. Therefore, we subtract the amount of mud from the total mass to obtain f_{mud}. Second, mass concentration data showed that the true values of concentration for Bentonite and sand S1 are 5%–10% lower than the target values or some times even 40%, for S2. This is because (a) the turbulence in the tank was not high enough to keep all the sand in suspension, particularly S2 and (b) we later found that the mesh size of the glass fiber filter (0.7 μm) was slightly bigger than the smallest particle sizes of the clay (Table 2). This is the reason why f_{mud} and concentrations in Q2 and V_{set} cases were always noticeably different from the targeted values. Subsequently, for simplicity and convenience, the term f_{mud}, for example, 00%, 75%, 50%, 25%, and 0%, actually refers to a very loose range, and sometimes even overlap, of mud/sand fraction, rather than indicating an absolute number. For example, $f_{mud} = 75\%$ implies a range of f_{mud} from around 65% to 85% instead of exact 75%. Even without reaching exact targets, we still have a broad range representative of mud/sand-dominant environments. Third, mass concentrations from three 1 L water samples in each V_{set} condition were almost the same (variations around 3%), verifying the quantification of f_{mud} in V_{set}. All calculations, data analysis, and figures are based on the true values of f_{mud}, mass of Bentonite, S1, and S2 in the mixture and total concentrations obtaining from physical water samples.

3. Derivation of Empirical Functions

In Pearson et al. (2021), we tested and validated a new concept, the Sediment Composition Index (SCI), in which the concentration of mud/sand in suspension could be derived from optical and acoustic measurements, that is, $SCI = 10\log_{10}(OBS_{signal}) - ADV_{signal}$. The present paper further develops the SCI concept, aiming to quantify mud/sand concentration. This section uses data from Q_{set} to demonstrate how f_{mud} and total concentration can be obtained from one pair of raw, uncalibrated optical and acoustic signals. First, only one pair of optical/acoustic signals is used for demonstration. Then, the application of the same procedure to all optical turbidity/acoustic pairs is discussed.

3.1. Approach

The hypothesis under investigation is that because acoustic sensors are more sensitive to coarse sediments and optical sensors are more sensitive to mud, the sediment sensitivity differences can be used to elucidate the fraction of mud/sand in the mixture when both optical and acoustic sensors are combined in one measurement. Figure 2 reveals the relationships of signal-signal and signal-concentration in Q_{set}. For better illustrations and simplicity, data from one pair of optical turbidity/acoustic sensor (O_{700}-A_8 or Wetlabs_FLNTU and LISST-ABS), out of 30 pairs from Q1 were used in Figure 2. Three observations can be made from this example. First, in Figures 2a–2c and 2e pure mud (Q1_100) and pure sand (Q1_0) conditions are always the boundaries of mixed mud/sand conditions
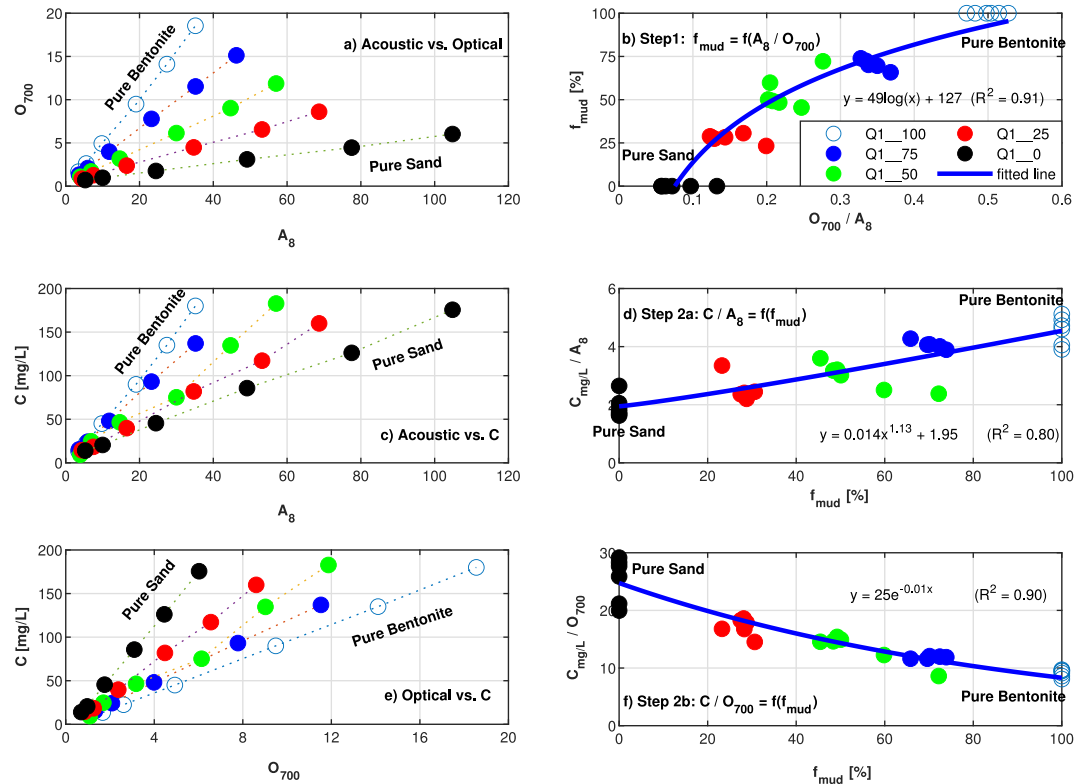
Figure 2. An example of relationships between O_{700} and A_8 (Optical 700 nm and Acoustic 8 MHz) and total concentrations. Only quantification set for sand S1 (Q1) data were used in this demonstration. Step 1, 2a, 2b: please refer to Equations 1–3.

and lean toward the optical/acoustic axes, confirming that optical turbidity/acoustic sensors indeed respond better to finer/coarser sediments, respectively. Second, there is a linear relationship between signal-signal (Figure 2a) and signal-concentration (Figures 2c and 2e) of the same f_{mud}, for example, five lines uniquely associated with five mud/sand ratios f_{mud}. In other words, the signal magnitudes of both sensors increase with the increase of concentration, yet the ratio of the optical/acoustic signal or concentration/signal remains constant. Third, theoretically, all the lines should converge to the point (0,0), which represents conditions with clear water, no turbulence shear, and no sediment. This is essentially the case in our experiments. These observations suggest that there are strong and unique relationships among raw signals, concentrations, and f_{mud}. This paper adopted the Curve Fitting Tool, provided by Matlab, to derive the relationship between signals, concentrations and f_{mud}. It is worth noting that the Curve Fitting Tool allows different functions, for consistency across all combination of sensors, we decided to choose the functions that provide highest R^2 rather than predefine a function form for a certain relationship.

Figure 2a shows the relationships between raw, uncalibrated signals of O_{700} and A_8 from Q1. Note that the output of A_8 is in mg/L by default. The sensor was not calibrated. As can be seen, each line in Figure 2a is associated with a certain slope or f_{mud}, indicating that the ratio of raw signals of O_{700}/A_8 is independent of concentration and only depends on the fraction of mud/sand in suspension. Subsequently, Figure 2b was produced by plotting f_{mud} against O_{700}/A_8 ratios to obtain Equation 1. Equation 1 demonstrates that the fraction of mud/sand in a suspension can be estimated from raw signals of O_{700} and A_8. Figures 2c and 2d shows the results when applying a similar procedure to A_8 signals and concentrations. A linear relationship between A_8 signals and concentrations is also seen. Equation 2 is then achieved based on the relationship between ratio of C/A_8 signals and f_{mud}, where C is the total concentration (mg/L). The same approach is applied to suspended concentrations and O_{700} signals (Figures 2e and 2f), to get Equation 3.

$$f_{mud} = 49\log_{10}(O_{700}/A_8) + 127 \quad (R^2 = 0.91) \tag{1}$$

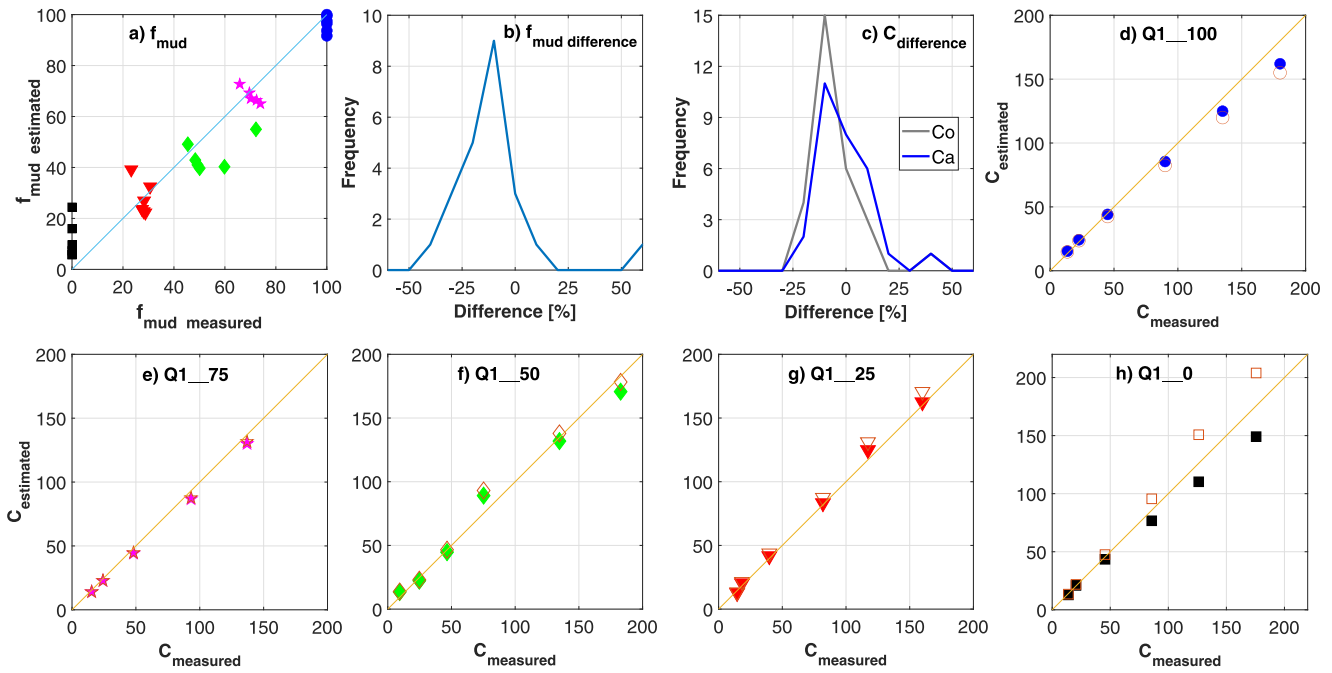$$(C/A_8) = 0.014f_{mud}^{1.13} + 1.95 \quad (R^2 = 0.80) \tag{2}$$

Figure 3. Differences between estimated and measured of f_{mud} and total concentration for the pair O_{700}, A_8. Ca: empty markers. Co: filled markers. Differences are calculated as $X_{difference} = \frac{(X_{estimated} - X_{measured})}{X_{measured}} 100\%$, where X denotes f_{mud} or C.

$$(C/O_{700}) = 25e^{-0.01f_{mud}} \qquad (R^2 = 0.90) \tag{3}$$

Equations 1–3, offer two ways to calculate total concentration. Starting with one pair of raw optical/acoustic signals.

- **Step 1:** obtain f_{mud} via Equation 1.
- **Step 2:** f_{mud} then can be substituted to
  Step **2a**: use Equation 2 to obtain Ca = $A_8 * (0.014f_{mud}^{1.13} + 1.95)$
  Step **2b**: use Equation 3 to obtain Co = $O_{700} * (25e^{-0.01f_{mud}})$

In this manuscript, steps **Step 1** and **2a** refer to a procedure in which the concentration, **Ca**, is calculated based on f_{mud} and the acoustic signal of the pair. For example, Equations 1 and 2 are the application of such procedure to the pair (O_{700}, A_8). Likewise, steps **Step 1** and **2b** refer to a similar procedure using f_{mud} and the optical signal of the pair (O_{700}, A_8) to calculate the concentration, **Co**, as in Equations 1 and 3. Thus, we denote SCI-Qx-Cy to refer to the procedure (steps 1 and 2a/2b) in which SCI functions (Equations 1 and 2 or Equations 1 and 3) were derived from the data set Qx and were used to estimate Cy where *x* indicates the data set, Q1, Q2 or Q12 and *y* indicates Ca or Co. Ideally, Ca and Co should be the same as they are both predicting total concentration.

3.2. Application: Single Pair (O_{700}-A_8)

This section further examines the reliability and accuracy of the SCI functions. Estimated f_{mud} and total concentrations were acquired by applying Equations 1–3 to Q1 data (Figure 3). Figure 3 illustrates the differences, $X_{difference} = \frac{(X_{estimated} - X_{measured})}{X_{measured}} 100\%$, where *X* denotes f_{mud} or C, respectively. In general, the SCI functions underestimate f_{mud}, and concentration by 10% (Figures 3a–3c). There are two potential explanations for these underestimations. First, for pure mud and pure sand conditions, the differences between optical and acoustic signals are at their largest magnitudes. This is because in pure mud conditions, the optical signal is at its highest value, whereas the acoustic signal is at its lowest value. The opposite trend is seen in pure sand conditions, where the acoustic sensor is much more sensitive to changes in concentrations of sand than the optical sensor. Hence, the errors in predictions of f_{mud} in these two particular cases are relatively high, especially with extremely low or extremely high concentrations, leading to accumulated errors throughout the calculation process (Figures 3d and
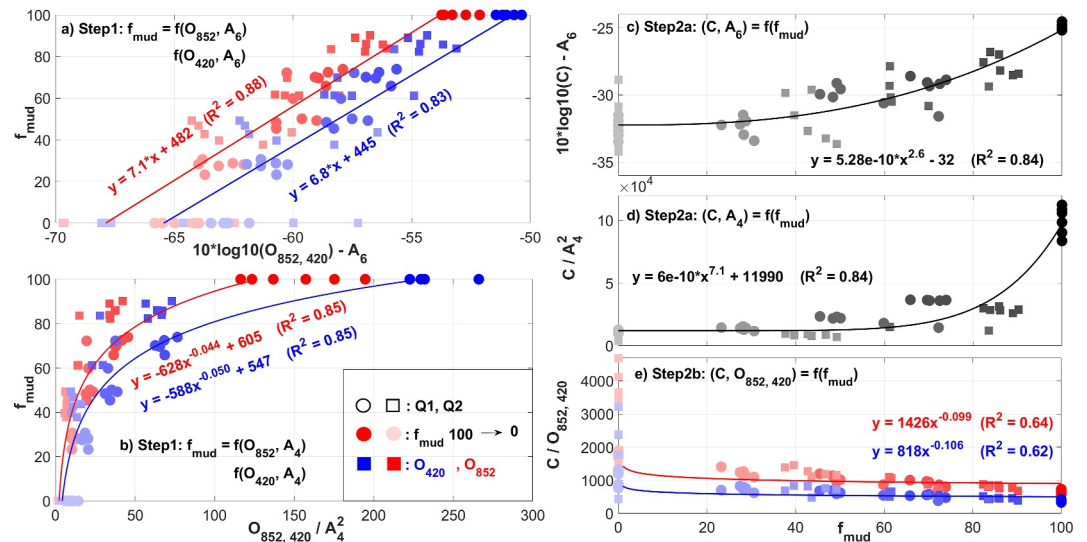
Figure 4. Application of SCI method to four optical/acoustic pairs with all data in Q_{set} (Q12). The reductions of f_{mud} from 100% to 0% are shown by the darkest color to lightest color. Blue: data from O_{420}. Red: data from O_{852}. The displayed functions are obtained from data set Q12.

3h). Second, the mathematical forms, for example, log (Equation 1), power (Equation 2), exponential (Equation 3), or linear are an important factor that impacts the performance of the method. Conducting a thorough sensitivity analysis of each different mathematical form on the overall accuracy of the SCI method is out of the scope of this paper. For simplicity and consistency, we decided to choose the function that provides the highest R^2. Readers are referred to Pearson et al. (2021) for additional information of how different functions, especially hyperbolic tangent function, dictate the performance of the method. Figure 3 also shows that the Co (Step 2b) approach provided slightly better results compared to Ca (Step 2a) approach. Specifically, Figure 3c reveals that the histogram of estimated concentrations in percentages of Co is sharper with a smaller standard deviation than that of Ca. Figures 3e–3g also reveals these differences between the two ways of calculation, albeit the differences seem to be insignificant for this pair of O_{700} and A_8.

3.3. Application: All Pairs

In the previous section, the pair (O_{700}-A_8) was used as an example to explicate the procedure of (a) derivation and calibration of SCI functions, (b) calculation of f_{mud}, and (c) calculation of total concentrations, Ca and Co. In this section, the same procedure is applied for other pairs of optical/acoustic signals as well as experimental data Q12 (all combinations are in the Supplementary Information).

Figure 4 summarizes the results of four pairs (O_{852} - A_6) (O_{420} - A_6) (O_{852} - A_4), and (O_{420} - A_4). Overall, Figure 4 shows similar patterns between signal-f_{mud} and signal-concentration as seen in Figures 2b–2d and 2f in which different f_{mud} is associated with one unique ratio of optical/acoustic signal. Unlike Figures 2 and 4 used data from both Q1 and Q2 experiments. Hence, the SCI functions were derived based on the combined behaviors of S1 and S2. It is also reminded that all the sensors are working concurrently, measuring the same suspension at very similar elevation in the water column. As such, Figure 4 provides important information regarding the behavior of optical/acoustic sensors to different SPM compositions. First, for the same type of acoustic device, the SCI functions are in similar forms (Figures 4a and 4b); yet, with different coefficients depending on the SPM compositions, the wavelengths and frequencies, as well as the working mechanisms of the sensors. For example, a closer examination of Figures 4a, 4b and e shows that the SCI functions are influenced by different wavelengths and frequencies to a greater degree than they are by particle sizes. That means that without prior knowledge of the particle sizes (S1 or S2), it is possible to use the "averaged" SCI function, that is, derived from Q12, to estimate f_{mud} and total concentration (of Q1, Q2, or Q12). Second, Figures 4a and 4b illustrate that moving from longer to shorter wavelengths will shift the SCI functions to the right or down. Third, due to the differences in principles of operation, the SCI functions are also different, for example, between A_6 and A_4 in comparison to O_{852} and O_{420}.
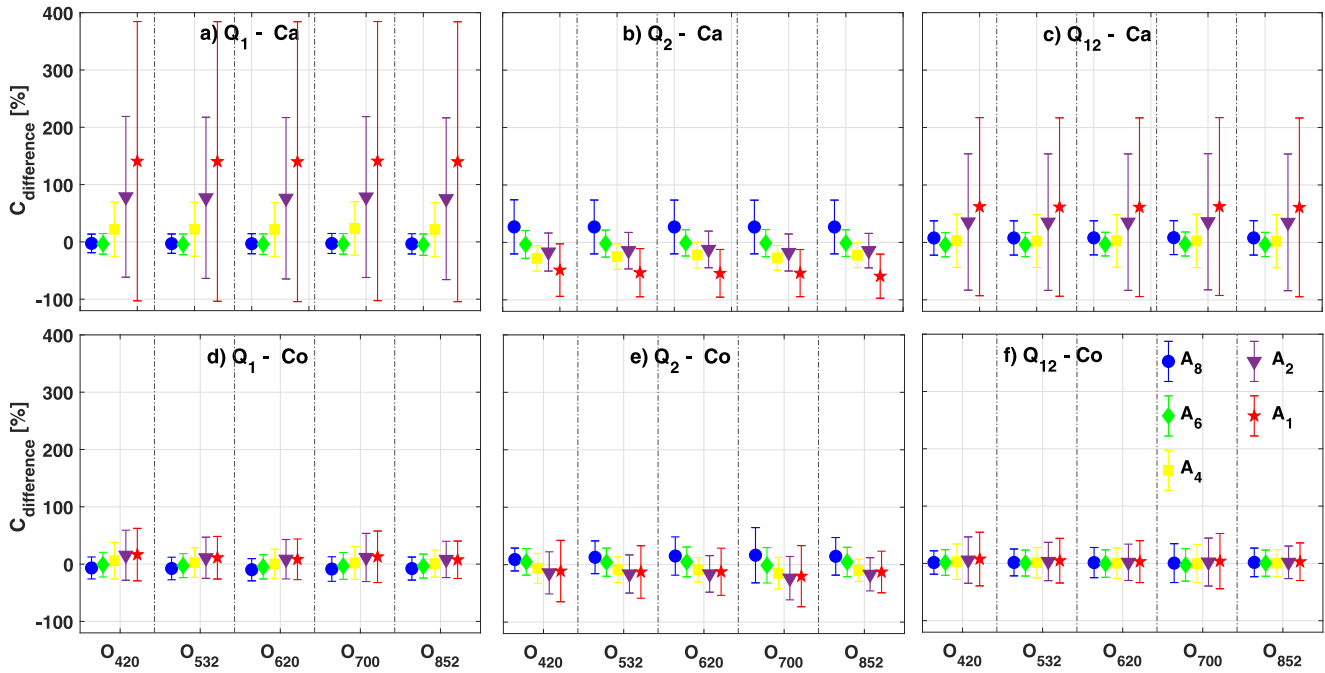
Figure 5. Comparison of all pairs when applying SCI-Q1 (a), (d), SCI-Q2 (b), (e), and SCI-Q12 (c), (f) functions to estimate Ca (steps 1 and 2a) and Co (steps 1 and 2b). Concentration differences, in %, between Ca, Co and $C_{measured}$. $C_{difference} = \frac{(C_{estimated} - C_{measured})}{C_{measured}} 100\%$. Markers: mean values, error bars: one standard deviation.

For example, Section 2.2.1 points out that the relationships between optical-A_6 is a log-linear and between optical-A_4 is a power function. This is one of the main issues when applying the SCI functions to wider range of different sensors.

Figure 5 further examines the results from Q_{set}. Figure 5 presents the differences in percentage between true and estimated concentrations, that is, between Ca, Co, and $C_{measured}$ obtained by SCI functions derived from Q1 (Figures 5a–5d), Q2 (Figures 5b–5e), and Q12 (Figures 5c and f), respectively. In Figure 5, the markers represent the mean values and the error bars represent one standard deviation of the population. The lower panel (SCI-Co) is plot in the same scale of the upper panel (SCI-Ca) for easier comparison; yet, note that the absolute values of the error bars sometimes reach to 50% or more. Figure 5 reveals that SCI-Co method across all pairs is more consistent and accurate than that of SCI-Ca. In other words, there is no remarkable difference between different optical turbidity sensors, and thus wavelengths are not a critical parameter in our case (Figure 5 lower panel). In contrast, the choice of acoustic frequencies dictates the accuracy substantially, for example, at 1, 2 MHz (Figure 5 upper panel). This is also the reason why Optical–$A_{0.5}$ pairs were not included in Figure 5: they over/underestimated f_{mud} and concentration in several orders of magnitude. According to Rayleigh regime, this is expected because lower frequencies are much less sensitive to the sands used in the experiments (d_{50} = 110 and 240 µm). It also explain why the performance of SCI-Ca_A2 and SCI-Ca_A1 are considerably better when they were calibrated with bigger sand size in Q2 (Figure 5b) rather than with smaller sand size in Q1 (Figure 5a). This observation will be discussed further in Section 5.

4. Validation

Unlike Q_{set}, in V_{set} we conducted experiments with mixtures of Bentonite, S1, and S2 at different fractions (Table 2). The V_{set} allows us to verify (a) the size-dependency of SCI functions and (b) whether the SCI functions, derived from Q_{set}, are applicable to a broader range of conditions. There are two notes associated with Figure 6. First, results from Q_{set} show that the pairs optical-A_1 provide much less accurate estimations. Hence, optical-A_1 pairs were excluded in this analysis. Second, V_{set} conditions 4 and 5 from Table 2 (or Figures 6d and 6e), are quite similar due to the uncertainties in controlling the amount of S2 which was partially deposited during the experiments. Nevertheless, V_{set} successfully creates distinctive SPM concentrations with different ratios of Bentonite, S1, and S2.
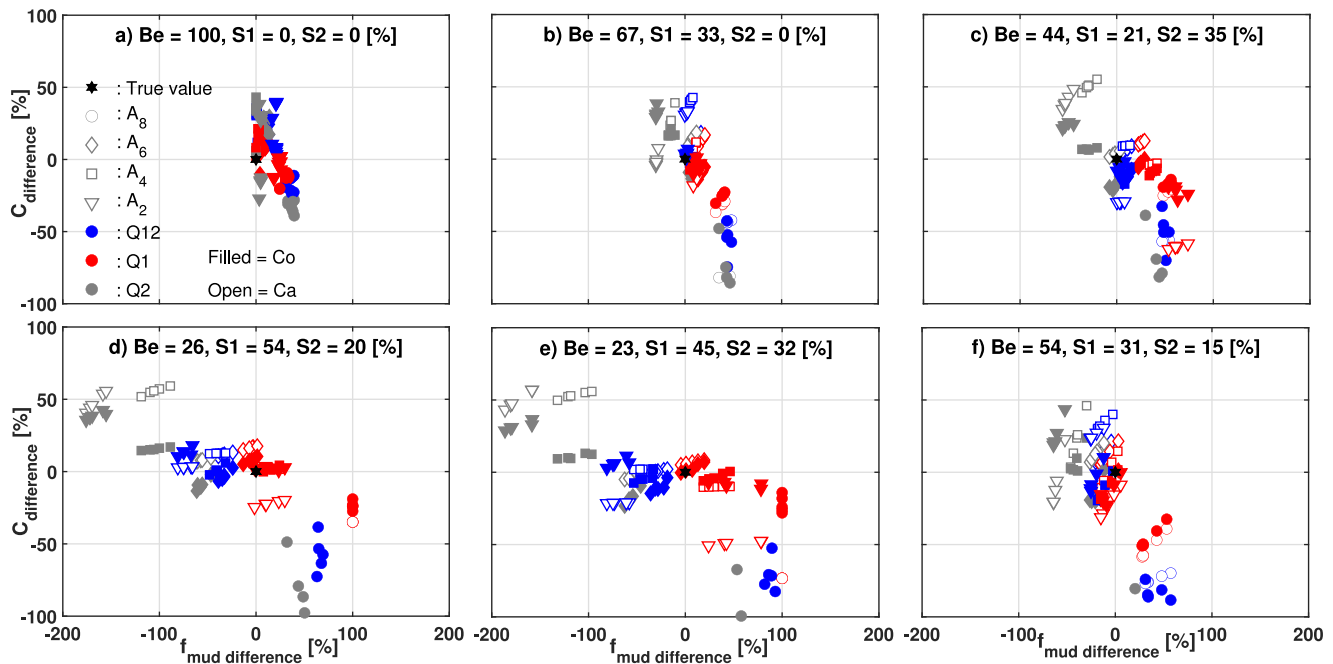
Figure 6. Application of SCI functions, derived from Q_{set}, to V_{set} data. The sub-figures show results from all pairs of each experimental condition. The legend should be read as a combination of marker + color + filled/open. Where filled marker = Co, empty marker = Ca. For example, a blue-filled-diamond means Co was obtained by $Q12$-$(O_{800 \to 420}$—$A_6)$ functions. Differences are calculated as $X_{difference} = \frac{(X_{estimated} - X_{measured})}{X_{measured}} 100\%$, where X denotes f_{mud} or C.

Figure 6 displays the error (or accuracy), in percentage, when applying the SCI functions derived from Q_{set} to V_{set} data. In general, SCI-optical functions (filled markers) are present in all conditions, confirming that this method is accurate and practical. Another observation is that whether or not SCI functions can reasonably predict f_{mud} depends heavily on the percentage of Bentonite in the mixture. For example, an increase in the absolute amount of coarser sediment leads to decrease in the accuracy of f_{mud} calculation (Figures 6a–6f).

In Figure 6, we consider the SCI functions that are readily applicable to field data only if they are able to predict both f_{mud} and C within the range of ±10% (Figure S2 in Supporting Information S1 for better visualization). In such cases, Figures 6a and 6b, representing a mud-dominated environment, show that SCI-Q12 and SCI-Q1 functions offering adequate estimations. When the mixture becomes coarser, S2 dominant, as in Figure 6c, the best SCI functions change to SCI-Q2-acoustic, that is, more open, gray markers presented. This is because acoustic sensors capture the changes in sand sizes better than optical turbidity sensors do, particularly for sand S2. Similarly, in S1 dominant conditions, Figures 6d and 6e, SCI-Q1 functions have the best performances.

5. Discussion

5.1. SCI and Field Measurements

Two prominent benefits make the SCI method stand out in comparison with other field measurement practices (Agrawal et al., 2019; Downing, 2006; Thorne & Hurther, 2014). First, it allows researchers to take advantage of the historical data to acquire new meaningful information, that is, the fraction and concentration of mud/sand in suspension. In long-term sediment dynamics monitoring, both optical turbidity and acoustic sensors are often used together (Fettweis et al., 2019; Fugate & Friedrichs, 2002; Pearson et al., 2021; Sahin et al., 2017; Voulgaris & Meyers, 2004). However, they are treated as individual measurements and are calibrated separately for different purposes. For example, an ADV or ADCP is often deployed to measure flow conditions. On the other hand, OBS is used for SPM concentrations. As shown in Section 3 and 4, the SCI method is able to provide the percentage of mud/sand, and hence, the proportion of mud and sand concentrations in suspension, respectively. Such information will provide crucial input and validation data to improve the performance of current sediment
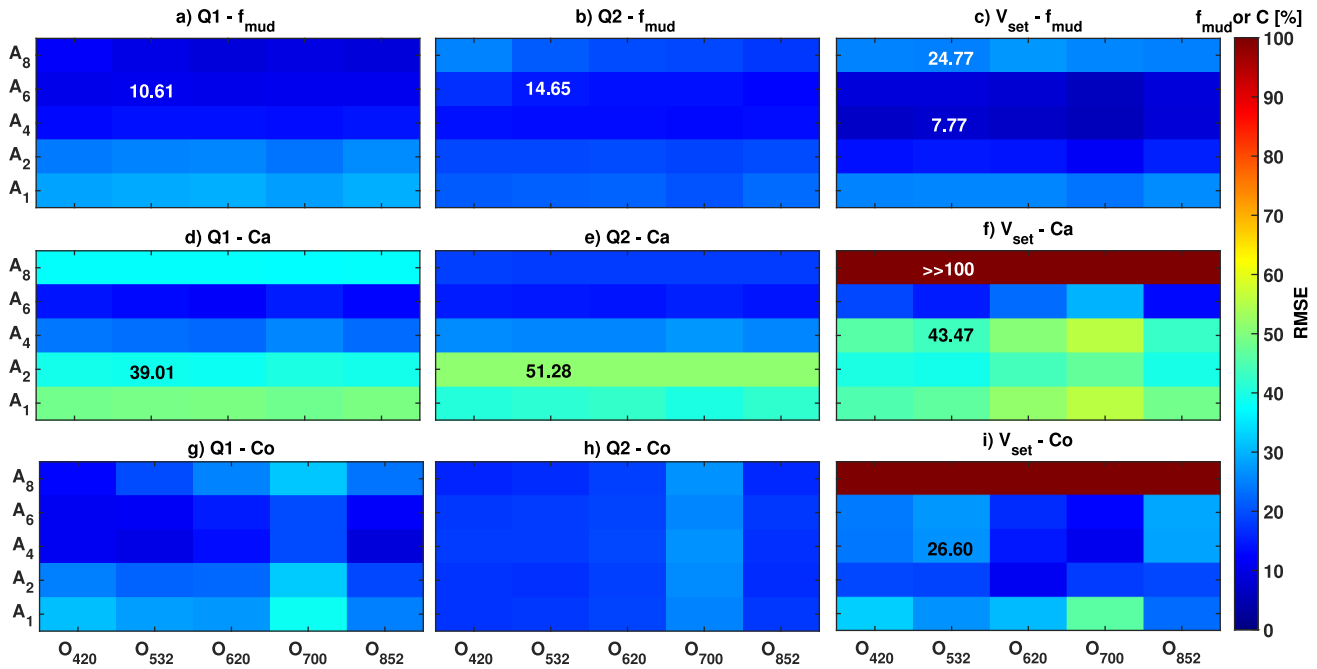
Figure 7. RMSE of the application of SCI-Q12 functions to data sets Q1, Q2, and V_{set}. RMSE $= \sqrt{(X_{estimated} - X_{measured})^2}$, where $X = f_{mud}$ or concentration. A few numbers associated with specific color are also given for better references. In this figure, SCI functions derived from data set Q12 were applied to calculate Ca (steps 1 and 2a) and Co (steps 1 and 2b) of different data sets, that is, from bimodal to multimodal particle size mixtures.

transport models, for example, for 2D models relying on data obtained from profilers like ADCP. Projects related to port dredging and beach nourishment also directly benefit from long-term mud/sand dynamics data.

Second, the SCI method allows the use of customized paired sensors. Using five different instruments with different wavelengths and frequencies, this paper showcased the procedure of how SCI functions can be derived and applied. In practice, SCI functions can be directly obtained from field measurements with the pair of optical turbidity/acoustic sensors of interest. Although integrated optical-acoustic sensors, for example, (Agrawal et al., 2019), have been developed, a key advantage of the SCI calculation is that it can rely on pairs of existing sensors that are already frequently deployed together in the field, without requiring a dedicated additional instrument. Specifically, at least three, preferably five, water samples from a deployment which covers the spring-neap tidal cycle should be used to provide detailed data on mud/sand fraction and total mass concentration. For pure mud conditions, one should take water samples at a calm period, for example, minimum wave and current during the neap tide (Pearson et al., 2021). The other samples should be taken at mild and energetic conditions when sand is more likely to be resuspended. These five data points can then be utilized to find the SCI functions as in Step 1 and Step 2a, 2b (Figures 2b–2 d and 2f). If the water sample data is already available from previous deployments, the SCI functions can be formulated with ease.

5.2. Frequency/Wavelength and Particle Size

This section further discusses the applications of SCI functions in the context field measurements where the contents of particle size and SPM are often unknown. V_{set} is a test of schematic mixtures that might be observed in field measurements, offering a much more complicated environment compared with Q_{set} from which the SCI-Q12 functions were derived. V_{set} provides double the range of concentrations and different ratios of Be, S1, and S2 in comparison to Q_{set}. Figure 7 shows the RMSE, indicating how well, the SCI-Q12 functions work under bimodal (Q1 and Q2) and multimodal (V_{set}) particle size distribution environments. Visually, higher acoustic frequencies (>4 MHz) often result in better estimation compared to lower acoustic frequencies (1 and 2 MHz). Regarding V_{set}, SCI-Q12 functions correctly reproduce the mud/sand fraction with 8%–26% uncertainty for frequencies from 2 to 6 MHz (Figure 7c).

The applications of SCI-Q12-acoustic (Figures 7d–7f), however, generate erroneous outcomes (>50%) except for optical-A_6 pair (Figure 7f). There are a few notes concerning the performance of the SCI-Q12 functions. It is clear that the accuracy declines with the increase of complexity of the mixtures, that is, from Q_{set} to V_{set}. Additionally, instead of 30 data points as in Q1 and Q2, there are only six data points in V_{set} (Table 2). Hence, the weight of one error is exaggerated and somewhat skews the RMSE calculation. The low sensitivity of sensor O_{700} and A_8 at lower concentrations also plays an important role in reducing the performance of the SCI-functions.

The finding that optical-A_6 pair is one of the best combinations becomes clear when put in the context of scattering theory, that is, $2\pi r\lambda^{-1} \approx 1$ (Downing, 2006; Haalboom et al., 2021; Thorne & Hurther, 2014). The optimal particle diameters for acoustic at frequencies 4 and 6 MHz are 120 and 180 μm, respectively. If we calculate a hypothetical mean particle diameter for each condition in V_{set} as $d_{avg} = \sum_i^n d_i p_i$ where d_i is the particle size of size fraction i (Bentonite = 40, $S1$ = 110, $S2$ = 240 μm), and p_i is the percentage by mass of size fraction i (Table 2). The results show that the values of d_{avg} vary from 40 to 136 μm which is just around the optimal working ranges of frequencies 4–6 MHz. This might explain why SCI-optical-$A_{4,6}$ functions almost always produce the most accurate predictions in both Q_{set} and V_{set}. Application of the same theory helps to explain why lower frequencies, <2 MHz, sometimes generate errors in prediction by several order of magnitude, because those frequencies are only sensitive to much larger particle sizes. The miscalculation of SCI-optical-A_8 pairs for V_{set}, however, is not easy to explain since the sensor A_8 only provides final output in the form of mass concentration without revealing the inversion function used or the raw signal. The differences between $Ca_{estimated}$ and $C_{measured}$ escalate with the increase of sand size, concentration and complexity degree, that is, multimodal size distribution, of the suspension. Therefore, one possible conclusion from Figures 6 and 7 is that A_8 sensor does not work properly under multimodal and/or coarser sand particle environments.

In a relatively different pattern, optical sensors are quite consistent and offer much lower variations in f_{mud} and total concentration predictions. Further investigation of coefficient of variations (standard deviation/mean) shows that optical sensors are more sensitive to the change of f_{mud}, while acoustic sensors are more sensitive to the change of particle sizes. For example, at the same concentration, changing from pure mud (f_{mud} = 100%) to pure sand condition (f_{mud} = 0%) results in a reduction in O_{700} signal of ≈34%, but only about 14% for A_6 signal. In contrast, the signal differences between S1 and S2 conditions for O_{700} is almost 14.8%, while for A_6 is ≈25%. Thus, the homogeneity or complexity of the mixture are not as important for optical sensors as for acoustic sensors.

Last but not least, it is worth mentioning that sand particles and floc aggregates dictate the corresponding optical/acoustic signals via their size, shape, density and/or color (Downing, 2006; Sahin et al., 2017; Thorne et al., 2007). In other words, sand particles and floc aggregates of the same size will behave differently because they are also different in density, shape and color, that is, the optical and/or acoustic scattering coefficients are different. Our previous study, Pearson et al. (2021) showed that for such cases, in both laboratory and field settings, the functionality and application of SCI-functions still hold. This is because both optical/acoustic signals altered, but the ratio between them remains constant.

5.3. Multi-Frequency or Multi-Wavelength

A question of interest is whether the same procedure is applicable to two paired optical sensors or two paired acoustic sensors of different wavelengths/frequencies. Inversion of multi-frequency acoustic backscatter data to obtain sediment size and concentration profile often requires some prior knowledge of the suspension and a suitable computational algorithm (Lynch et al., 1994; Moate & Thorne, 2009; Thorne et al., 2021; Thorne & Hurther, 2014). The present study does not intend to make comparison between our approach and other existing methods. Rather, we would like to discuss a possible way to take advantage of multi-wavelength and/or multi-frequency measurements to achieve similar results. Figure 8 highlights a few examples of combinations of different wavelengths/frequencies. While no useful information could be extracted from optical-optical pairs (Figure 8), the relationship between multi-frequency measurements is very promising, alike Figures 4c and 4d. For example, in Figures 8a–8c, a certain slope or intercept associated with each condition also holds for a specific mud/sand ratio. Differences between finer and coarser sand particle sizes are seen in some cases (Figures 8a–8c). Nevertheless, providing a full calculation for SCI-acoustic-acoustic functions is out of the scope of this study. In future, this approach will be further investigated.
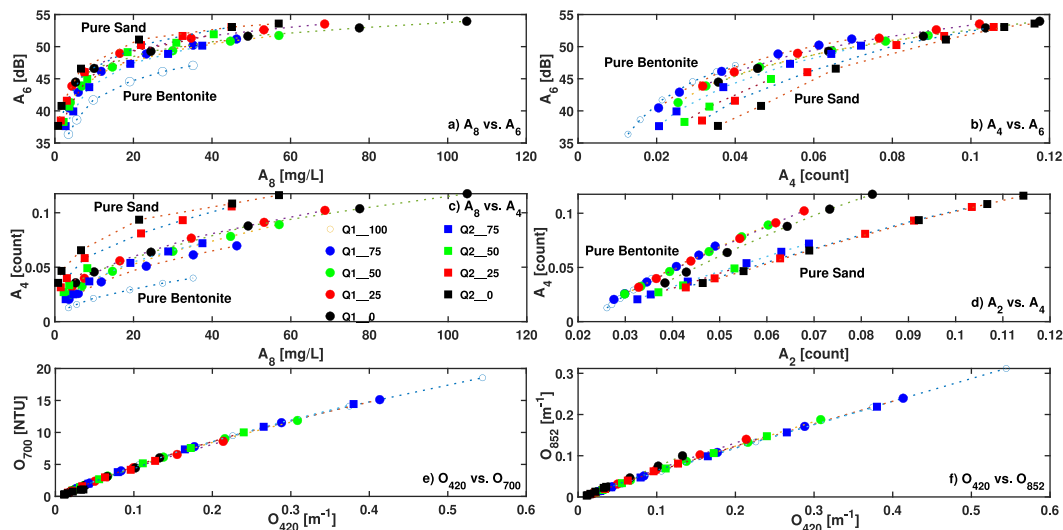
Figure 8. Examples of combinations of acoustic-acoustic, and optical-optical pairs. The two upper panels show similar pattern as seen in Figure 2, indicating that it is possible to derive a similar SCI functions from acoustic-acoustic data set, that is, sub-figures a, b, c All signals are raw, uncalibrated.

6. Conclusions

This study proposes a new approach to obtain mud/sand fraction and the total concentration of a suspension based on conjugating optical-acoustic measurements. Two sets of experiments, providing bimodal (Q_{set}) and multimodal (V_{set}) particle size distributions, are used to calibrate and validate our SCI functions. In general, SCI-Co functions (Steps 1 and 2a), have a better performance than their counterpart SCI-Ca functions (Steps 1 and 2b). The results show that for suspension in which the particle size is known that is, SCI functions were chosen accordingly, predicted concentrations can be as accurate as ≈ 10 mg/L (Figures 7d and g). Without prior knowledge of particle sizes, SCI functions derived from Q12 can be applied to various sediment mixtures with a reasonable error, that is, <10% for f_{mud} and <15% for concentration. For example, considering there is an average size for each condition in V_{set} the best optical-acoustic pairs are optical wavelength 620–700 nm and acoustic frequency 4–6 MHz. The results suggest that the SCI method is highly applicable to sedimentary-dynamic environments, for example, estuaries and coastal zones, even without sensor calibrations and knowledge of mud/sand ratio. In the near future, the possibility of applying the same approach to multi-frequency acoustic measurements and a larger range of concentrations as well as different types of minerals and particle sizes will be investigated.

Data Availability Statement

The experimental data used in the study are available at https://zenodo.org/doi/10.5281/zenodo.12819148 with open access (Tran et al., 2024).

References

Agrawal, Y., Pottsmith, H., Dana, D., & Mikkelsen, O. (2019). Super-turbidity meter: Lisst-aobs combines optical turbidity with acoustics. *Proceedings of the 38th IAHR World Congress*, *38*, 1–6.

Aquatec Subsea Ltd (2012). Application Note AN4 - Inversion technique. AN4Rev1.0.

Bux, J., Peakall, J., Rice, H. P., Manga, M. S., Biggs, S., & Hunter, T. N. (2019). Measurement and density normalisation of acoustic attenuation and backscattering constants of arbitrary suspensions within the Rayleigh scattering regime. *Applied Acoustics*, *146*, 9–22. https://doi.org/10.1016/j.apacoust.2018.10.022

Chmiel, O., Baselt, I., & Malcherek, A. (2018). Applicability of acoustic concentration measurements in suspensions of artificial and natural sediments using an acoustic Doppler velocimeter. *Acoustics*, *1*(1), 59–77. https://doi.org/10.3390/acoustics1010006

Downing, J. (2006). Twenty-five years with OBS sensors: The good, the bad, and the ugly. *Continental Shelf Research*, *26*(17), 2299–2318. https://doi.org/10.1016/j.csr.2006.07.018

Doxaran, D., Leymarie, E., Nechad, B., Dogliotti, A., Ruddick, K., Gernez, P., & Knaeps, E. (2016). Improved correction methods for field measurements of particulate light backscattering in turbid waters. *Optics Express*, *24*(4), 3615. https://doi.org/10.1364/oe.24.003615

Druine, F., Verney, R., Deloffre, J., Lemoine, J., Chapalain, M., Landemaine, V., & Lafite, R. (2018). In situ high frequency long term measurements of suspended sediment concentration in turbid estuarine system (seine estuary, France): Optical turbidity sensors response to suspended sediment characteristics. *Marine Geology*, *400*, 24–37. https://doi.org/10.1016/j.margeo.2018.03.003

Fettweis, M., Riethmüller, R., Verney, R., Becker, M., Backers, J., Baeye, M., et al. (2019). Uncertainties associated with in situ high-frequency long-term observations of suspended particulate matter concentration using optical and acoustic sensors. *Progress in Oceanography*, *178*, 102162. https://doi.org/10.1016/j.pocean.2019.102162

Fugate, D. C., & Friedrichs, C. T. (2002). Determining concentration and fall velocity of estuarine particle populations using ADV, OBS, and LISST. *Continental Shelf Research*, *22*(11–13), 1867–1886. https://doi.org/10.1016/s0278-4343(02)00043-2

Haalboom, S., de Stigter, H., Duineveld, G., van Haren, H., Reichart, G. J., & Mienis, F. (2021). Suspended particulate matter in a submarine canyon Whittard Canyon, Bay of Biscay, NE Atlantic Ocean: Assessment of commonly used instruments to record turbidity. *Marine Geology*, *434*, 106439. https://doi.org/10.1016/j.margeo.2021.106439

Hoitink, A., & Hoekstra, P. (2005). Observation of suspended sediment from adcp and obs measurements in a mud-dominanted environment. *Coastal Engineering*, *52*(2), 103–118. https://doi.org/10.1016/j.coastaleng.2004.09.005

Livsey, D. N., Turner, R. D. R., & Grace, P. R. (2023). Combining optical and acoustic backscatter measurements for monitoring of fine suspended-sediment concentration under changes in particle size and density. *Water Resources Research*, *59*(8), 1–20. https://doi.org/10.1029/2022wr033982

Lynch, J. F., Irish, J. D., Sherwood, C. R., & Agrawal, Y. C. (1994). Determining suspended sediment particle size information from acoustical and optical backscatter measurements. *Continental Shelf Research*, *14*(10–11), 1139–1165. https://doi.org/10.1016/0278-4343(94)90032-9

Moate, B. D., & Thorne, P. D. (2009). Measurements and inversion of acoustic scattering from suspensions having broad size distributions. *Journal of the Acoustical Society of America*, *126*(6), 2905–2917. https://doi.org/10.1121/1.3242374

Moura, M. G., Quaresma, V. S., Bastos, A. C., & Veronez, P. (2011). Field observations of SPM using ADV, ADP, and OBS in a shallow estuarine system with low SPM concentration-Vitória Bay, SE Brazil. *Ocean Dynamics*, *61*(2–3), 273–283. https://doi.org/10.1007/s10236-010-0364-5

Pearson, S. G., Verney, R., van Prooijen, B. C., Tran, D., Hendriks, E. C., Jacquet, M., & Wang, Z. B. (2021). Characterizing the composition of sand and mud suspensions in coastal and estuarine environments using combined optical and acoustic measurements. *Journal of Geophysical Research: Oceans*, *126*(7), e2021JC017354. https://doi.org/10.1029/2021jc017354

Sahin, C., Verney, R., Sheremet, A., & Voulgaris, G. (2017). Acoustic backscatter by suspended cohesive sediments: Field observations, seine estuary, France. *Continental Shelf Research*, *134*, 39–51. https://doi.org/10.1016/j.csr.2017.01.003

Salehi, M., & Strom, K. (2011). Using velocimeter signal to noise ratio as a surrogate measure of suspended mud concentration. *Continental Shelf Research*, *31*(9), 1020–1032. https://doi.org/10.1016/j.csr.2011.03.008

Slade, W. H., Boss, E., & Russo, C. (2011). Effects of particle aggregation and disaggregation on their inherent optical properties. *Optics Express*, *19*(9), 7945–7959. https://doi.org/10.1364/oe.19.007945

Sutherland, T. F., Lane, P. M., Amos, C. L., & Downing, J. (2000). The calibration of optical backscatter sensors for suspended sediment of varying darkness levels. *Marine Geology*, *162*(2–4), 587–597. https://doi.org/10.1016/s0025-3227(99)00080-8

Thorne, P., Agrawal, Y., & Cacchione, D. (2007). A comparison of near-bed acoustic backscatter and laser diffraction measurements of suspended sediments. *Oceanic Engineering, IEEE Journal of*, *32*(1), 225–235. https://doi.org/10.1109/joe.2007.890978

Thorne, P. D., & Hurther, D. (2014). An overview on the use of backscattered sound for measuring suspended particle size and concentration profiles in non-cohesive inorganic sediment transport studies. *Continental Shelf Research*, *73*, 97–118. https://doi.org/10.1016/j.csr.2013.10.017

Thorne, P. D., Lichtman, I. D., & Hurther, D. (2021). Acoustic scattering characteristics and inversions for suspended concentration and particle size above mixed sand and mud beds. *Continental Shelf Research*, *214*, 104320. https://doi.org/10.1016/j.csr.2020.104320

Tran, D., Jacquet, M., Pearson, S., van Prooijen, B., & Verney, R. (2024). Estimation of mud and sand fractions and total concentration from coupled optical-acoustic sensors. *Zenodo*. [Dataset]. https://doi.org/10.5281/zenodo.12819148

Tran, D., Jacquet, M., Pearson, S., & Verney, R. (2021). *Investigating suspended particulate matters from multi-wavelength optical and multi-frequency acoustic measurements* (Vol. 2021). EGU.13022.

Voulgaris, G., & Meyers, S. T. (2004). Temporal variability of hydrodynamics, sediment concentration and settling velocity in a tidal creek. *Continental Shelf Research*, *24*(15), 1659–1683. https://doi.org/10.1016/j.csr.2004.05.006